Theor Chem Acc (2007) 117:1041–1059
DOI 10.1007/s00214-006-0219-9

REGULAR ARTICLE

Light driven molecular switches: exploring and tuning their photophysical and photochemical properties

Piero Altoè · Fernando Bernardi · Irene Conti · Marco Garavelli · Fabrizia Negri · Giorgio Orlandi

Received: 20 July 2006 / Accepted: 13 October 2006 / Published online: 22 December 2006

Abstract In recent years, computational photochemistry has become a valid tool for the investigation of photophysical properties and photochemical reaction mechanisms in organic chromophores. Theoretical chemists can now adapt their tools to the subject under investigation and to the type and accuracy of the desired information. Different computational strategies can now be adopted to characterize different aspects of the photoinduced molecular reactivity of a given chromophore and to provide, in principle, a quite detailed description of the reactive process from energy absorption to photoproducts formation. The basic aim is to establish a correlation between the structure of the molecule and its photochemical outcome, and, in particular, to assess the effect of modifications of the chromophore and of the molecular environment. In this perspective, recent advances and applications of photoinduced cis $\rightleftarrows$ trans isomerizations involving some organic chromophores active in biologically or technologically relevant problems is reviewed here and discussed in the light of new results. In particular, the photochemistry of azobenzene, retinals and of the green fluorescent protein chromophore is considered, taking into account structural changes and environment effects. The results presented in this work are intended to be the first step toward the design of chromophores that can act as molecular photoswitches.

Keywords Quantum chemistry · Photochemistry · Molecular switches · Azobenzene · Green fluorescent protein · Retinal

1 Introduction

The performance and the properties of a material can be related to the structure and behavior of its constituting molecules. Progress in this direction has become more and more relevant in recent years. In general, the better we are capable of modifying the molecular properties in the desired way, the more we are able to tailor the proper material that will fit our purposes and needs. In this respect, the design of *molecular devices* that respond in the desired way to certain external stimuli, such as light and electrons, represents a challenging and promising task in *nanotechnology*, that is, in molecular technology [1].

Among molecular devices, those based on reversible photochemical reactions attract a great interest and will be discussed here. These devices operate upon irradiating with light of wavelength required to excite the component molecules to electronic states that trigger the photochemical process. In principle, the fine design of the proper reactive molecule, allows for a direct control of the photoreaction outcome and of the reagent's photostability. The latter property is also very important, because, in practical applications the photoreaction of the device needs to be repeated a large number of times [2–5]. It is apparent that the elucidation of the

F. Bernardi deceased on 20th February 2006.

P. Altoè · F. Bernardi · I. Conti · M. Garavelli · F. Negri (✉) · G. Orlandi
Dipartimento di Chimica 'G. Ciamician',
Universita' di Bologna, Via F. Selmi, 2, 40126 Bologna, Italy
e-mail: fabrizia.negri@unibo.it

P. Altoè · I. Conti · F. Negri · G. Orlandi
INSTM, UdR Bologna, Bologna, Italy

factors controlling photochemical reactions is necessary for the rational design of the photoreactive material. To achieve this goal, the role of *theoretical photochemistry*, based on efficient computational methods and strategies, is extremely important.

In this paper, we discuss some of our recent works in this area which aims at following the course of the photochemical reaction through the construction and characterization, with state-of-the-art ab initio methods, of the so called "photochemical reaction path" or "pathway approach" [6,7]. This is a minimum energy path (MEP) [8], starting at the reactant structure and developing on the potential energy surfaces (PES) of the photochemically relevant states. Such interstate path originates on the optically active electronic excited state at the ground state equilibrium geometry, where the absorption takes place most efficiently, because of the favorable Franck Condon (FC) factor, and it ends at the ground state photoproduct valley after crossing several PES. The ultimate goal is the complete description of what happens at the molecular level *from energy absorption to product formation*. In this approach, the attention is focused on the topological properties of the PES such as slopes, minima, saddle points, barriers, crossings between states [conic intersections (CIs)] and in general funnels. In this way the calculated path describes, strictly, the motion of *a vibrationally cold molecule* moving with infinitesimal momentum. While in general this path does not represent a "real" trajectory (it does only when the vibrational relaxation is faster than the photoprocess itself), it allows a qualitative rationalization of different experimental data such as the excite-state lifetimes, the nature of the photoproducts and, more qualitatively, the quantum yields and transient absorptions and emission spectra. Alternative and more demanding approaches consider also the dynamic aspects of photoreactions by computing trajectories [9,10] or by describing the motion of the centre of a wave packet along the potential energy surfaces [11].

A strong motivation for this theoretical study comes from the recent advances in femtosecond spectroscopy and ultrafast techniques [7], often combined with single molecule studies, which provide highly resolved time dependent data, shedding light on the several processes, occurring on different time scales, in the course of the photoreaction [7].

Photochemical processes may be tuned by environment effects (e.g., solvent, protein cavity, and so on), and by minor modifications in the chromophore structure. The tuning may result in changes of the energies and ordering of excited states and in the relative energies of the key geometries, such as barriers and CI. Similar modifications of the PES may be induced also by steric effects that may thereby control the decay rate and photochemical outcome.

In this work, we discuss the *cis–trans* isomerization photoreactivity of azobenzene in different excited states and compare it with the properties of a modified azobenzene obtained by saturating two C=C double bonds in one benzenic ring. In a similar way, we report recent results for the retinal chromophore, on the effect of protein environment in rhodopsins and finally, we discuss the solvent and protein effects on the green fluorescent protein (GFP) chromophore. Particular attention is paid to the interplay between photophysical and photochemical properties. To this end, optical properties [absorption energies, IR, Raman and resonance Raman (RR) intensities] are also computed. In particular, the tight relationship between RR intensities and the first step in the deactivation mechanism is underscored by the prototypical example provided by the GFP chromophore.

All the chromophores considered in this work have an extended conjugated π-system and are characterized by ultrafast and efficient *cis–trans* photoisomerizations. These systems can be employed, potentially, in nanotechnology for the design and construction of molecular devices such as random access memories, photon counters, picosecond photo detectors, neural-type logic gates, optical computing, light-switchable receptors and sensors, light addressable memories and molecular motors [2,12,13].

2 Methods

Fully unconstrained MEP computations from non-stationary structures (such as the FC and the CI points) have been used to characterize the reaction coordinate of the photoinduced processes and have been performed according to the prescriptions described in Ref. [14,15]. Briefly, this is accomplished, first, via locating an initial direction of relaxation (IRD) on the PES (as close as possible to the non-stationary point) [14,15], and, second, via standard minimum energy path computations following that IRD. An IRD corresponds to a local steepest descent direction, in mass-weighted Cartesians coordinates (mwcc), from a given starting point. The IRD is calculated by locating the energy minimum on a hyperspherical (i.e., $n-1$ dimensional) cross-section of the n dimensional potential energy surface (n is the number of vibrational degrees of freedom of the molecule) centered on the starting point (e.g., the FC point). The radius of this hypersphere is usually chosen to be small [typically 0.25–0.5 au in mwcc (au = $\mathrm{amu}^{1/2}\mathrm{a}_0$)] in order to locate the steepest direction in the vicinity of the starting point (i.e., the hypersphere center). The IRD is

then defined as the vector joining the starting point to the energy *hyperminimum*. Once the *hyperminima* have been determined, the associated minimum energy path (emerging from these points) is computed as *the steepest descent line in* mwcc [the standard intrinsic reaction coordinate (IRC) method is used in this case] [16,17] using the IRD vector to define the initial direction to follow.

The general procedure adopted to compute MEPs is based on the use of the complete active space self consistent field (CASSCF) method in conjunction with the standard 6-31G* basis set. One important aspect is the careful selection of the CAS, whose dimension reflects the best compromise between chemical relevance of the included orbitals and computational efficiency. For azobenzene, we selected 14 electrons in 12 orbitals [CAS(14,12)]. This CAS is capable of describing with a good degree of accuracy both the ($n\pi^*$) and the ($\pi\pi^*$) states [18]. In particular, we verified that the two occupied and the two empty orbitals removed from the active space have an occupation very close to 2 and 0, respectively, for the electronic states of interest. For the investigated retinal chromophore models the full space of π electrons and π orbitals was considered. For the model chromophore of GFP we selected 12 electrons in 11 orbitals out of the 16 π electrons and 14 π orbitals. One of the three excluded orbitals is localized on the amidic nitrogen, while the remaining two correspond to the highest and lowest energy π-orbitals of the benzene ring [19].

Energies of the optimized CASSCF points are corrected via single point CASPT2 computations. The combined ab initio CASPT2 [20,21] // CASSCF [22–25] methodology has been extensively used since it has been proven to guarantee a satisfactory accuracy [7,26].

Implicit solvent effects are taken into account through the polarizable continuum model (PCM) [27–29] method. More specifically, the effect of solvent on photoexcited reaction paths was computed at CASSCF level, through the PCM method, and energies were corrected via single point CASPT2 computations.

Explicit solvent and protein environments are described using an in-house developed version of the quantum mechanics/molecular mechanics (QM/MM) method. (Altoe et al. in preparation) Several hybrid QM/MM schemes have been developed, depending on the coupling between the QM and MM parts and on the description of the boundary between the QM and MM regions. Here, we adopt an energy subtraction method for the energy partitioning (following the ONIOM scheme [30]) and we describe the QM/MM boundary with a second generation link atom approach, where hydrogen atoms are used to saturate the dangling bonds of the QM fragment and the point charges on the MM boundary atoms are redistributed on neighbouring atoms to avoid unphysical polarization. The MM contributions are evaluated with AMBER [31] using the generalized AMBER force field (GAFF) [32] whilst the QM contributions are generally computed at CASSPT2//CASSCF.

If we label "model-H" the H-capped QM fragment and "real" the entire system formed by the QM and MM regions, the QM/MM Hamiltonian reads:

$$\hat{H} = \hat{H}^{\text{model-H}}_{\text{QM,ch}} + \hat{H}^{\text{real}}_{\text{MM.0}} - \hat{H}^{\text{model-H}}_{\text{MM,0}}$$

where $\hat{H}^{\text{model-H}}_{\text{QM,ch}}$ is the QM Hamiltonian of "model-H" embedded in the electrostatic field produced by the MM point charges (original Amber parametrization). This term ensures that polarization effects are taken into account on the QM fragment, that is, at QM level. The second term, $\hat{H}^{\text{real}}_{\text{MM,0}}$ is the MM energy of "real", in which the charges of the QM region are set to zero, and $\hat{H}^{\text{model-H}}_{\text{MM,0}}$ is the MM energy of "model-H" with all the charges set to zero. The last two terms include van der Waal's interactions and bonding terms (stretching, bendings, torsions) in the QM/MM boundary region described with the Amber force field.

The usual procedure consists in a full minimization of the MM region after each QM optimization step. During the minimization of the MM region the electrostatic interaction between the QM and MM parts is computed classically using, for the QM region, point charges derived from the QM wave function according to the CHELPG or ESP fitting schemes. The two layers scheme (QM + MM) outlined above, can be easily adapted to a three layers scheme ($QM + MM_1 + MM_2$) in which, the MM region is broken in two shells, MM_1 and MM_2, described classically and subject to different regimes of minimization.

3 Azobenzene and derivatives

Azobenzene (Ab) undergoes *cis* <–>*trans* (E<->Z) isomerization with respect to the central N=N bond. Two paths are possible and have been proposed as alternative reaction routes [33,34]: the torsion around the N=N double and the in-plane inversion, that is the increase of the NNC angle from ca. 120 to ca. 240 °. The reactive electronic states are the S_1 ($n\pi^*$) and the $S_2(\pi\pi*)$ states, which show in *n*-hexane absorption bands with maxima at 432 (440) and 318 (260) nm, respectively, for the E (Z) form [35]. The lifetimes of these states are very short, 500 and 110 fs for S_1 and S_2, respectively [36].

Excitations on S_1 ($n\pi^*$) and $S_1(\pi\pi^*)$ in acetonitrile lead to different photoisomerization yields: $\phi(Z \rightarrow E) = 0.55$ and $\phi(E \rightarrow Z) = 0.31$ for excitation of S_1, and $\phi(Z \rightarrow E) = 0.35$ and $\phi(E \rightarrow Z) = 0.14$ for excitation of S_2 [37]. Similar yields are found in different solvent [38]. The different photoisomerization rates in S_1 ($n\pi^*$) and $S_2(\pi\pi*)$ imply that the Kasha rule does not apply to this molecule and, thus, arise the interesting problem of the paths followed by the decay of the $S_2(\pi\pi^*)$ state, as indicated in Fig. 1. Furthermore, while the two photoisomerization yields of S_1, which add to 0.86, a value close to 1, are compatible with a common photoreactive intermediate, the two photoisomerization yields $\phi(Z \rightarrow E)$ and $\phi(E \rightarrow Z)$ of S_2, which add to 0.49, must be associated with different reaction routes.

The sensitized photoisomerization, taking place on the T_1 state, occurs only in the direction $Z \rightarrow E$: the quantum yield of the $Z \rightarrow E$ photosensitized photoisomerization is close to 1, while the yield of the opposite process is 0.015 [37].

Several studies of the S_0, S_1 and T_1 potential energy surfaces, in particular along the torsion and the inversion coordinates, of the isolated Ab molecule have been performed to identify the most efficient decay and isomerization routes [18,39–42]. The dynamical effects on the photoisomerization on the S_1 surface has been computed by Persico and coworkers [9,10].

In a previous work we have computed the MEPs for the photoisomerization on S_0, T_1 and S_1, including transition states and S_1/S_0 CIs [18]. The results are collected in Fig. 2. In the following, we discuss the photiosomerization of Ab in its different electronic states, including also the S_1 ($\pi\pi^*$) state.

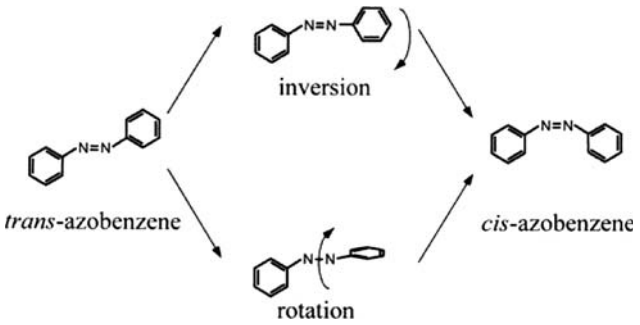

Fig. 1 Torsional and inversion pathways for Azobenzene isomerization

3.1 S_0 and T_1 photoisomerization pathways

The quantum yield of the $Z \rightarrow E$ photosensitized photoisomerization on T_1 PES is close to one, while the yield of the opposite process is 0.015 [37] and the T_1 lifetime is assumed to be very short because it has so far not been observed. Qualitatively, these facts can be accounted for in terms of the energy curves of Fig. 2, which shows that the S_0 and T_1 MEPs cross and that the lower energy S_0/T_1 crossing is the one on the E side and is almost degenerate with the T_1 minimum. In Ref. [41], the optimized CASPT2 S_0 and T_1 potential energy curves along

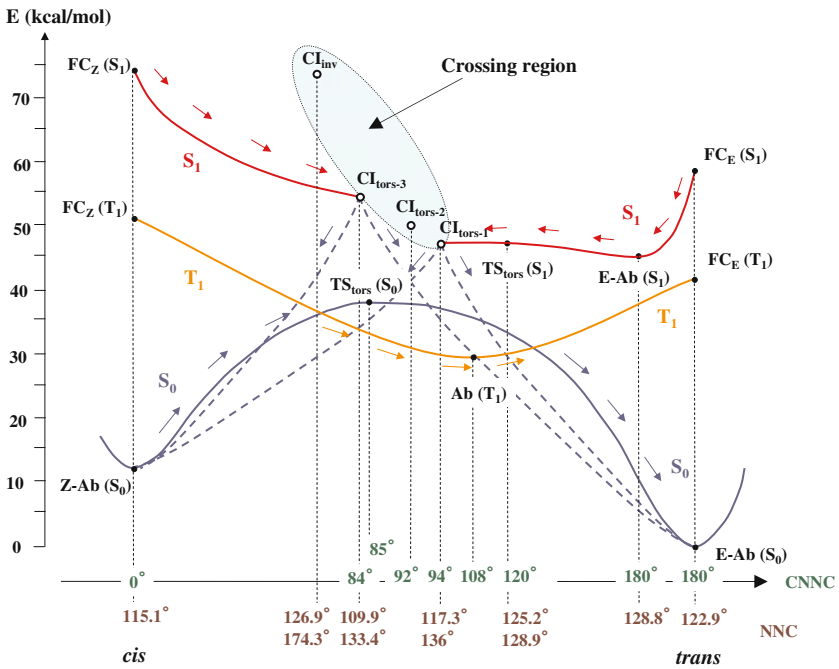

Fig. 2 Singlet (S_0 and S_1) and triplet (T_1) reaction paths for the $E \rightarrow Z$ isomerization in azobenzene. Energy profiles are schematized for sake of clarity and are scaled to match CASPT2 values. *Full (open) circles* represent stationary and Franck–Condon points (S_1/S_0 Conical intersections). The *horizontal axis* represents the CNNC torsion coordinate (*green numbers*) and NNC (*brown numbers*). The *shaded region* highlights the S_1/S_0 crossing space. The paths of T_1 and S_1 radiationless decays are also shown (adapted from Ref. [18])

the CNNC torsion coordinate were calculated with 10° steps and in this section we shall use these results.

According to CASPT2 calculations [41], the S_0 potential energy curve *along the CNNC torsion coordinate* shows a barrier of 38.1 kcal/mol, at $\phi = 90°$, while the T_1 potential energy curve presents a minimum at lower energy, 28.8 kcal/mol at $\phi = 100°$. The two curves cross at $\phi = \phi_1 = 68°$ and $\phi = \phi_2 = 105°$. The energy of the former crossing, which is closer to the Z form, amounts to 32.0 kcal/mol, while, the energy of the latter crossing is 28.9 kcal/mol, only 0.1 kcal/mol above the T_1 minimum.

The energy of the S_0 barrier *along the inversion path* is 40.5 kcal/mol and the energy of the T_1 minimum is 48.4 kcal/mol. Therefore the two energy curves along the inversion do not cross. Thus, the Ab molecule can easily cross from S_0 to T_1, or viceversa, in the twisted region, but not in the inverted region.

The Ab molecule, once it is excited in T_1 at the E or Z geometry, proceeding on the MEP follows the torsion pathway reaching the the two $S_0 - T_1$ crossings at ϕ_1 and ϕ_2 from where it decays to S_0 thereby isomerizing. Also *cis–trans* thermal isomerization can occur via the T_1 state by overcoming a barrier of about 32 kcal/mol, which corresponds to the higher $S_0 - T_1$ crossing, provided that the $S_0 - T_1$ spin-orbit (SO) coupling, V_{so}, is sufficiently strong.

The V_{so} interaction in Ab is much larger than the typical values of the S_0-$^3\pi\pi^*$ SO couplings of planar aromatic compounds (0.05 cm^{-1}), because it gets a large contribution from one-center terms due to the $n\pi^*$ character of T_1. The calculated couplings between S_0 and two of the three T_1 components at 68 and 105° amount to 19.8 and 22.8 cm^{-1}, respectively [18], large enough to justify the short lifetime of T_1.

The rate, k, of the $T_1 - S_0$ inter-system crossing (isc) process, occurring at the S_0/T_1 crossings, can be evaluated according to the Fermi golden rule [43]

$$k = (4\pi^2/h)V_{SO}^2 \rho F \tag{1}$$

where ρ is the density of active vibrational states of the final electronic state, F is the FC factor, ρF is the density–weighted FC factor and V_{so} is the $S_0 - T_1$ spin-orbit coupling.

We have evaluated the ρF term, by assuming (a) that the dominant contribution to the FC factor comes from the CNNC torsion mode, ϕ, which is responsible of the T_1/S_0 crossings and (b) that the $T_1 - S_0$ isc occurs predominantly from the vibrational levels of T_1 corresponding to the T_1/S_0 crossings. In other words, we have adopted a model based on the high temperature limit approximation and on a single vibrational coordinate, ϕ.

The information about the T_1 and S_0 potential energy curves, $U_s(\phi)$ and $U_T\phi$, are taken from our previous work [41]. The $U_T(\phi)$ potential has been approximated as an harmonic function within an interval around its minimum at ϕ_0 including the two T_1/S_0 crossings

$$U_T(\phi) = (1/2)a(\phi - \phi_0)^2 \tag{2}$$

where $a = 19.2$ kcal/(mol rad^2) and $\phi_0 = 100°$. The two T_1/S_0 crossings occur at $\phi = \phi_1 = 68°$ (*cis* side) and $\phi = \phi_2 = 105°$ (*trans* side) and involve the activation energies of $E_{act} = 3.2$ kcal/mol and $E_{act} = 0.1$ kcal/mol, respectively.

The ρF term is evaluated by use of the Kubo and Toyozawa approach [44], which is related to the Landau–Zener equation and is appropriate for treating high-temperature processes. Accordingly, this term, multiplied by the Boltzmann factor, is given by

$$\rho F \cdot \exp(-E_{act}/kT) = \int_{\infty}^{\infty} \exp(-U_T/kT) \cdot \delta(U_T - U_S)\mathrm{d}\phi \Big/ \int_{\infty}^{\infty} \exp(-U_T/kT)\mathrm{d}\phi \tag{3}$$

and it is the sum of two contributions, one for each of the two S_0/T_1 crossings at ϕ_1 and ϕ_2

$$\rho F = \frac{\sqrt{a/2\pi kT}}{[\partial(U_T - U_S)/\partial\phi]_{\phi_1}} + \frac{\sqrt{a/2\pi kT}}{[\partial(U_T - U_S)/\partial\phi]_{\phi_2}}$$

Using the data of our previous work [41], we obtain $[\partial(U_T - U_S)/\partial\phi]_{\phi_1} = 32$ kcal/(mol rad) and $[\partial(U_T - U_S)/\partial\phi]_{\phi_2} = 42$ kcal/(mol rad).

Thus, the two contributions to ρF are 5.5×10^{-4} cm at the ϕ_1 crossing and 4.6×10^{-4} cm at the ϕ_2 crossing. The value between S_0 and two of the T_1 components is 20 cm^{-1}. Using the proper values for the V_{so} couplings, namely 19.8 and 22.8 cm^{-1}, at 68 and 105° respectively, the pre-exponential factors of the $T_1 \sim S_0$ isc rate constant of one of the active components of T_1 toward the *cis* and the *trans* sides are 2.5×10^{11} s^{-1} and 2.7×10^{11} s^{-1}, respectively.

Including the activation energy factor $\exp(-E_{act}/kT)$, at room temperature, the rate constants are $k = 2.5 \times 10^{11}$ s^{-1} and $k = 9.2 \times 10^8$ s^{-1} for $T_1 \sim S_0$ for the decay toward the *trans* and the *cis* forms, respectively. These results agree with the observation that the yield of the E → Z phosensitized isomerization is 10^{-2} times the yield of the reverse Z → E process [37].

Assuming that the three components of T_1 are equally populated, the rate of the $T_1 \sim S_0$ process is 2/3 of

the rate of one of the active T_1 components, that is, $1.6 \times 10^{11}\ s^{-1}$. The corresponding lifetime of 6 ps, which is very short for a T_1 state, provides an explanation for the lack of spectroscopic observation of the T_1 state of Ab.

The pre-exponential factor obtained for the rate of the inverse $S_0 \sim T_1$ process, leading from S_0 to the two active components of the state T_1, is $5 \times 10^{11}\ s^{-1}$. This rate is of the same size of the pre-exponential factors reported for the thermal Z–E isomerization of Ab ($1.95 \times 10^{11}\ s^{-1}$ from Ref. [34] and $8 \times 10^{10}\ s^{-1}$ from Ref. [45]. These findings support the idea that the thermal isomerization of Ab can proceed by the torsion mechanism via the $S_0 - T_1 - S_0$ non-adiabatic path involving the triplet state. Moreover, the calculated activation energy also is consistent with the value measured. In fact, since our calculated energy of the higher $S_0 - T_1$ crossing is 32 kcal/mol and the energy of the Z isomer is 12 kcal/mol, the resulting activation energy for the $Z \rightarrow E$ process is 20 kcal/mol. This value is in agreement with the activation enthalpy of 22 kcal/mol measured for the thermal isomerization [34].

3.2 S_1 photoisomerization pathway

The photoisomerization of Ab in the S_1 state was discussed previously [18,41]. After the molecule is excited in S_1 at the E structure ($\phi = 180°$), it proceeds along the MEP, which follows the CNNC torsion coordinate. On this torsion path, one transition state TS_{tors} (S_1) is found at about $\phi = 120°$, at an energy only 1.8 kcal mol^{-1} above the *trans* (E) isomer [18]. Moving toward the twisted geometry, the molecule reaches a hyperline of conic intersections in the twisted region. The lowest energy CI (CI_{tors-1}), occurring at $\phi = 94°$, is 2.2 kcal mol^{-1} above the S_1 minimum, and the molecule can decay from that CI to S_0, thereby isomerizing [18]. A recent work on the photodynamics of Ab in S_1 showed that the dynamic drive renders the photoisomerization feasible also for $\phi > 90°$ [10].

From the molecular structure at these CIs (CI_{tors-i}), it follows that torsion is the most important coordinate for the Ab photoisomerization in the state S_1 ($n\pi^*$). In fact, the S_1 photoisomerization path along the inversion coordinate would require a much higher energy, at least 20 kcal/mol above the E isomer [18], to reach CIs and thus its role on the S_1 decay is negligible. The low energy of the CIs in the twisted region explains the short lifetime [36,46] observed for S_1 and the sizeable yield of *cis–trans* isomerization.

When the molecule is excited in S_1 at the Z structure, the twisting path from there is barrierless and this feature accounts for the faster decay of the Z compared to the E isomer [36], as well as for the observed higher yield of the $Z \rightarrow E$ with respect to the $E \rightarrow Z$ photoisomerization process [37].

CIs along the inversion pathway have also been found (CI_{inv}), but these are at much higher energy (ca. 25 kcal mol^{-1} higher than the S_1 minimum of E–Ab) and are very unlikely to represent competing deactivation and isomerization channels for S_1.

3.3 S_2 photoisomerization pathway

In this section, we report preliminary results on the MEP, including transition states and S_1/S_0 CIs, and on the mechanism of decay and isomerization, following the excitation of Ab on S_2. These results were obtained at CASSCF and CASPT2 level with a 14/12 active space and the 6-31G* atomic basis set. The S_2 state, which is of $\pi\pi^*$ nature and belongs to the B_u symmetry species, has a large transition moment to ground state and is responsible of the most intense band in the visible-near UV with maximum at 318 nm ($\varepsilon_{max} = 22{,}300$) in hexane solution [35] and is similar to the S_1 state of stilbene.

Starting at the E structure, after the relaxation of the NN and CN bonds, the MEP on S_2 reaches, without requiring activation energy, the PES of another state that gets significant contributions of doubly excited configurations $n^2\ \pi^{*2}/\pi^2\ \pi^{*2}$. The latter state shows a deep minimum at the twisted geometry, confirming the results of Refs. [39] and [41]. On the Z side the picture is similar, but the doubly excited state keeps a significant component of $(n\pi^*)^2$ nature along the torsion coordinate.

On the PES of the state $S(n^2\ \pi^{*2}/\pi^2\ \pi^{*2})$ now defined S_2, we found a region of S_1/S_2 CIs parallel to the computed MEP and essentially degenerate to it. This region, extending from $\phi = 180°$ to $\phi = 123°$, is easily accessible from the S_2 MEP (predominantly the torsion coordinate) by moving orthogonally to it, along symmetric C–N=N *bending modes*, because of the small energy difference. Through this region of S_1/S_2 CIs the molecule decays in very short time to the state S_1 along the full $180° > \phi > 120°$ interval.

Once the molecule has reached the S_1 ($n\pi^*$) state, it will deactivate to ground state through an extended S_1/S_0 crossing subspace, which spans very different molecular structures going from the lowest energy fully-twisted C–N=N–C geometries to asymmetric C–N=N in-plane bent geometries (inversion channel) and to symmetric C–N=N bent structures. Molecules that have reached the S_1 state may intercept a S_1/S_0 crossing region well above the fully twisted structures, and thus a substantial fraction of them decays to the ground state leading to the formation of the reactant. This picture is in agreement with the smaller $E \rightarrow Z$ photoisomer-

ization quantum yield observed for the S_2 ($\pi\pi^*$) state (14%) with respect to the yield obtained exciting the S_1 ($n\pi^*$) state (31%) [37].

The decay of the S_2 ($\pi\pi^*$) *cis* isomer follows the same lines. The photoisomerization quantum yield (35%) is reduced with respect to the yield obtained exciting the S_1 ($n\pi^*$) state (55%) [37]. The S_2 quantum yield of the Z → E processes remains higher than the reverse E → Z processes because the MEP slope toward the twisted geometry is higher for the former processes and consequently the impulsive motion along torsional coordinate is more effective.

A more detailed report of these calculations is in preparation.

3.4 A modified azobenzene: cyclohexenylphenyldiazene

Because of the importance of azobenzene for applications, it is of interest to consider the effects of substituents or of structural modifications of Ab on its properties. It is well known that substituents, especially electron donors or acceptors, can change substantially the properties of Ab. Here, we present preliminary results on the effects of the modification of the aromaticity of one benzenic ring, namely of the saturation of two double bonds on the same ring, on the photophysical and photochemical properties.

The molecule obtained in this way, the cyclohexenylphenyldiazene (CPD), has an important difference with respect to Ab: it has no symmetry. Therefore, the classification of electronic states by symmetry is lost and the states in Ab belong to different irreducible representations and cannot interact, in CPD can interact and mix.

The second difference is due to the reduction of the π electron system in CPD. For this reason, to obtain the same accuracy as in Ab, a larger atomic basis set including diffuse orbitals is required. In spite of these differences, ab initio CASPT2//CASSCF with calculations employing the ANO-L (4s3p2d/3s2p) [47] basis set show that the lowest singlet states parallel those of Ab. In particular, MS-CASPT2 calculations at the ground state geometry of the E isomer find the energies in the $n\pi^*$ and $\pi\pi^*$ states, observed in absorption and responsible of the photoreactivity, at 58.1 and 112.9 kcal/mol.

The photoisomerization in the S_1 ($n\pi^*$) state takes place via the torsional pathway, essentially barrierless, and the S_1/S_0 CI is located close to the twisted geometry ($\phi = 90°$). Also in the ($\pi\pi^*$) singlet state the molecular deactivation appears to follow the same path as in Ab. Starting at the E structure, the MEP on S_2 crosses to the PES of the state based on the $n^2\pi^{*2}/\pi^2\pi^{*2}$ doubly excited configurations that has a deep minimum at the twisted geometry.

Moving on the PES of the S($n^2\ \pi^{*2}/\pi^{\ 2}\ \pi^{*2}$) state that has become S_2, the molecule intercepts a region of S_1/S_2 CIs, which, as in Ab, is easily accessible from the MEP by moving along C–N=N *bending modes*. Through this region of S_1/S_2 CIs the molecule decays very fast to the state S_1 along the full $180° > \phi > 130°$ interval and then it deactivates to ground state through an S_1/S_0 crossing subspace, spanning a variety of molecular structures. Since molecules on the S_1 state may intercept S_1/S_0 crossing region away from the fully twisted and the fully inverted structures, a substantial fraction of them can reach the ground state with formation of the reactant, as found for Ab. Completely similar results have been found for the decay of excited Z isomer of CPD.

In conclusion, in spite of the very different chemical structure, calculations suggest that CPD will show a similar photochemical behavior. Thus, partial saturations of a benzyl ring appear to represent a moderate perturbation of the spectroscopic and photophysical properties of Ab and, thus, may be a viable way to tune the Ab properties. A full account of these calculations will be given elsewhere.

4 Biological chromophores

4.1 Retinals

4.1.1 Isolated chromophores

The biological activity of rhodopsin proteins [48–53] is triggered by the ultrafast (200 fs in Rh) light-induced *cis–trans* isomerization of the retinal PSB chromophore, which induces a conformational change in the photoreceptor [48,52]. Recently, we have reported the results of a series of ab initio multiconfigurational second-order perturbation theory computations for PSB models of different chain length in isolated conditions (i.e., in vacuo). These include, among the others, the minimal PSB model 2-*cis*-penta-2,4-dieniminium cation **1** [54], the all-*trans*-epta-2,4,6-trieniminium cation **2** [55], and the 11-*cis* (PSB11) and all-*trans* (PSBT) retinal chromophore models 4-*cis*-γ-methylnona-2,4,6,8-tetraeniminium **3** and all-*trans*-nona-2,4,6,8-tetraeniminium **4** cations, respectively [7,56,57]. As reported in Ref. [7], photoisomerization path computations on models **1**, **2**, **3** and **4** have provided a unified and unambiguous (although qualitative) view of the *intrinsic* (i.e., absence of environmental effects) photochemical reactivity of PSBs. Despite the difference in the length of the conjugated chain (which quantitatively affects the spectros-

copy and the energetic of the system) and the lack of the retinal β-ionone ring (which could play a role in the steric factors involved in constrained environments), it has been demonstrated that, in all cases, the photochemically relevant state (driving the photochemistry of the system) is the spectroscopic charge-transfer state S_1 (that corresponds to the ^1B_u-like—hole-pair (i.e., zwitterionic)—spectroscopic state of polyenes). Moreover, the S_1 reaction co-ordinate along the computed barrierless photoisomerization path is curved, being sequentially dominated by two different perpendicular modes (see Fig. 3 for a schematic view of the shape of the S_1 potential energy surface of **3**). The first mode is totally symmetric (preserving the planarity of the system) and drives the initial (<50 fs) dynamics [58] out of the Franck–Condon point (FC) through a concerted double-bond expansion and single-bond compression process involving C–C bond order inversion. The second mode is asymmetric and is dominated by the *cis–trans* isomerization mode that ultimately leads to a conical intersection (CI) featuring a 90° twisted central double bond (see Fig. 4). The CI features a charge–transfer electronic structure corresponding to a twisted intramolecular charge transfer (TICT) state [7,54,59] where,

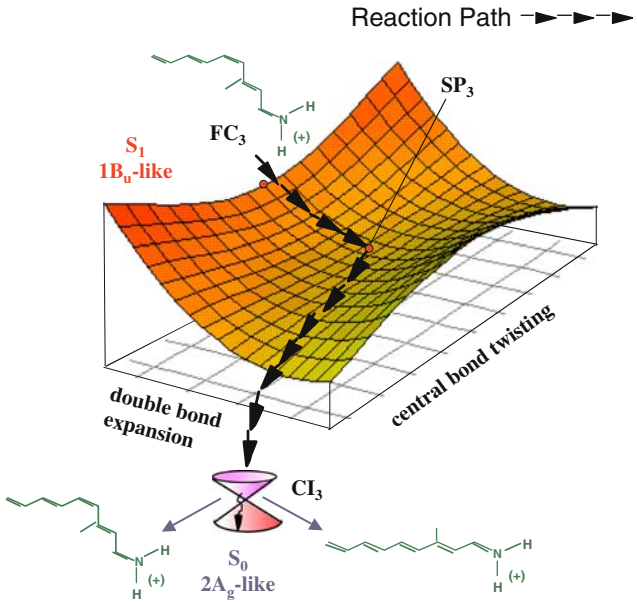

Fig. 3 Schematic illustration of the two-mode structure of the $S_1(1B_u$-like) energy surface along the excited state isomerization path for model 3

substantially, a "net" electron has been transferred from the "C" to the "N" end of the skeleton and, conse-

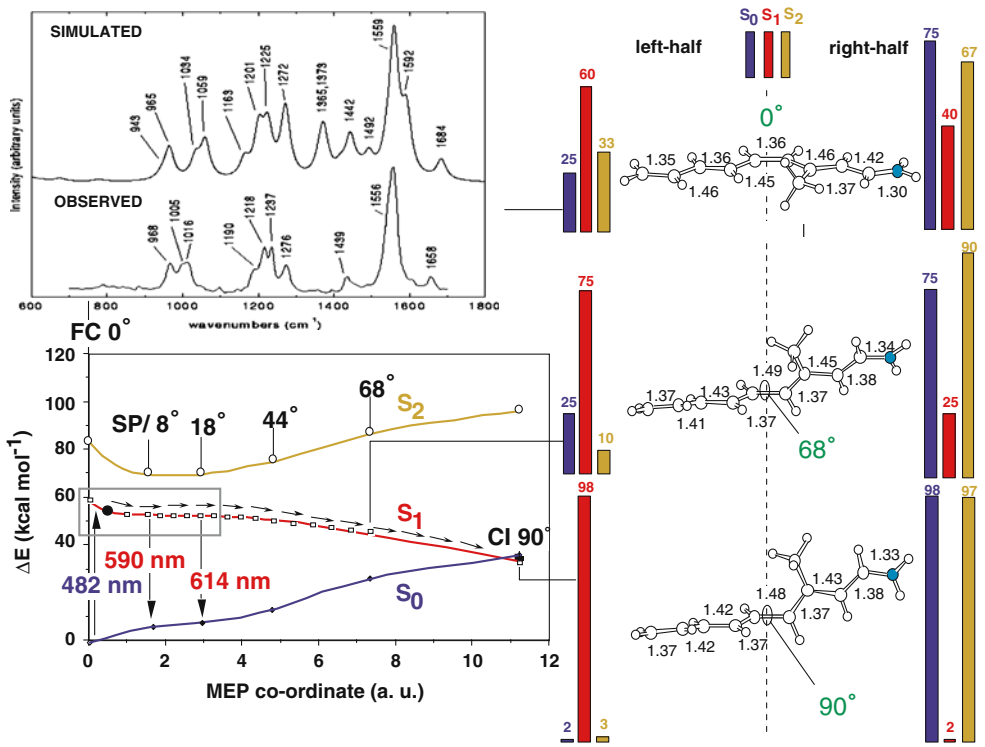

Fig. 4 Energy profiles along the S_1 reaction coordinate of the PSB11 model 3 (*open squares*) from the Franck–Condon point (FC) to the decay point CI (*conical intersection*). *Open circles and diamonds* show the S_2 and S_0 energy cross-sections along the same coordinate. The structures (geometrical parameters in Å and degrees) document the progression of the molecular structure along the coordinate, while the bar diagrams describe the change in the S_0, S_1 and S_2 Mulliken charges (as % unit of the net positive charge) of the C=C–C=C–C–(*left*) and –C–C=C–C=N (*right*) fragments. The *top–left* inset displays the observed and simulated RR spectra for PSB11 and model 3, respectively (adapted from Ref. [125])

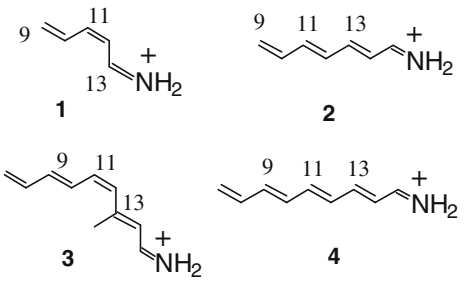

Formula 1

quently the positive charge has moved from "N" to "C". These data provide a rationale for the ultrafast radiationless decay observed in retinal chromophores (Formula 1–2).

Computed absorption and fluorescence maxima, changes in dipole moments and simulated resonance Raman spectra for model **3** [7,56,60,61]. (see Fig. 4) are consistent with the corresponding experimental quantities, providing a validation of the quality of the investigated models [62]: notice that the computed two-mode reaction coordinate of the S_1 relaxation path of retinal chromophores has now been validated experimentally [58,64–68] both in proteins and solvents.

4.1.2 Counterion Effects

Among others, the intermolecular interaction of the chromophore cation with its counterion (a carboxylate anion in proteins) must play a crucial role in determining the environment effects. In fact, as mentioned above, the photochemically relevant S_1 state is a "hole-pair" charge transfer state [7,54,56,59]. Thus, its relative energy and stability with respect to the "dot–dot" S_2 and S_0 covalent states must depend on the position of the counterion relative to the chromophore backbone. Pioneering studies and first qualitative models of counterion effects on retinal PSB photochemistry are due to Warshel [69], Birge, Nakanishi, Honig, Sheves [70,76] Michl and Bonacic-Koutecky [77,78]. Anyway, the lack of accurate ab initio computations and systematic investigations, has lead us to probe counterion effects at the CASPT2//CASSCF level for the positions/orientations defined by models **1a**, **1b**, **1c** and **2a**, **2b**, **2c**, **2d** [79]. Although the energetics delivered by these shorter retinal models may be quite different than for retinal itself, we still think that we can have a qualitatively correct picture for the effects of a countercharge (an acetate placed at ca. 3 Å distance) on the photochemistry and spectral tuning of PSBs in general, as we previously showed for PSBs in vacuo. We have shown that while these results provide information on the factors responsible for (i) the relative stability of the S_0, S_1, and S_2 states; (ii) the

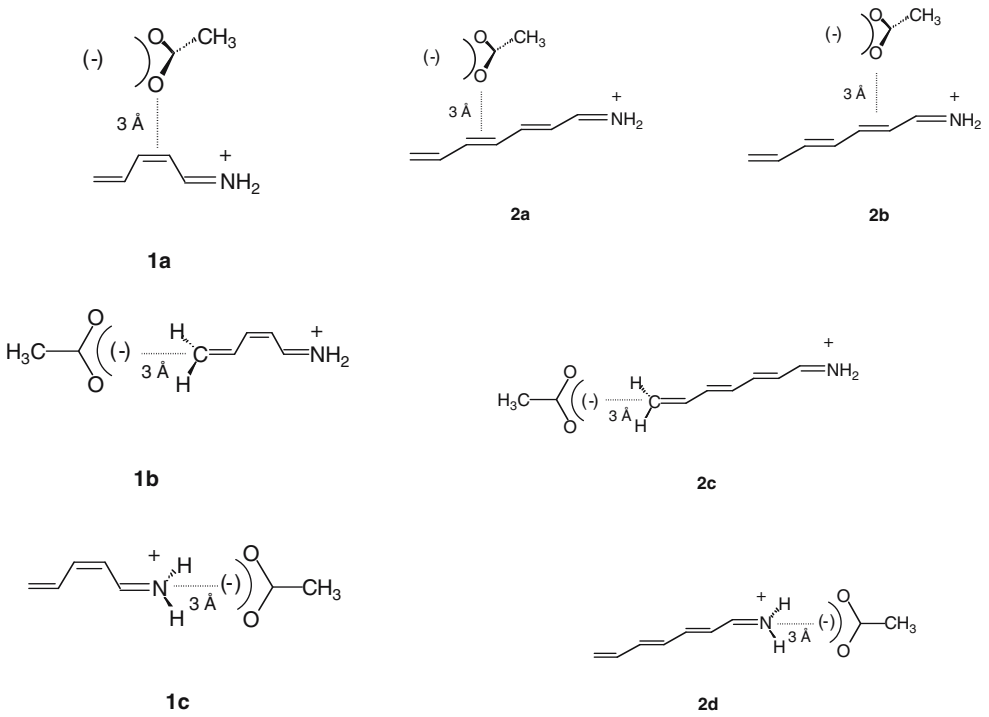

Formula 2

selection of the photochemically relevant excited state; (iii) the excited state lifetime and reaction rate and (iv) the control of the photoisomerization stereospecificity, a predictive and simple qualitative (electrostatic) model readily rationalizes the computational results providing an explanation for different aspects of the observed "environment" effect [79].

A qualitative electrostatic model: In Scheme 1, we report the structure of the singlet manifold along the computed S_1 reaction path for a PSB (here the penta-2,4-dieniminium cation has been used as a model) [7,54,56]. In the same scheme we also provide information on the electronic nature of the singlet (S_0, S_1, S_2) states. Accordingly, horizontal, smoothed colored bars (representing the PSB skeleton), illustrate the positive charge distribution as a function of the color intensity. Note that the initial steepness of the singlet excited states is higher for the covalent state S_2 (see also Fig. 4). There is general agreement of all multi reference methods that the covalent state energy is reduced much faster during geometrical relaxation [80–82].

If one places a counterion close to the chromophore, its electrostatic field will stabilize the singlet (S_0, S_1, S_2) states depending on the distance between the negative (counterion) and the positive (chromophore) charge centers. On the other hand, the position of the positive charge along the PSB backbone depends on the nature of the electronic state [e.g., it is closer to the nitrogen-head (*N-head*) for covalent states and to the carbon-tail (*C-tail*) for the charge-transfer state]. Thus, opposite counterion effects are expected of different states. Indeed, three different limiting cases can be envisioned:

1. The counterion is placed in a *Central* position above the chromophore backbone (**1a**, **2a**, **2b**). In this case the stabilization effect must be almost independent from the singlet state nature (i.e., the distance between the negative and positive charges is similar for covalent and charge–transfer states). Therefore, the structure of the singlet manifold is likely to remain substantially unchanged (see Scheme 1).
2. The counterion is placed closer to the *C-tail* (**1b**, **2c**). In this position (see Scheme 2), the charge–transfer (S_1) state is stabilized (i.e., shorter couterion/positive-charge distance) with respect to the (S_0, S_2) covalent states. This leads to a change in the structure of the singlet manifold where the $S_1 - S_0$ energy gap decreases (i.e., an absorption red shift) and the $S_2 - S_0$ increases. Consequently (according to the intensity of this effect and the slopes of the S_1 and S_0 surfaces) the S_1/S_0 crossing should occur earlier along the S_1 isomerization path.
3. The counterion is placed closer to the *N-head* (**1c**, **2d**). In this position, the covalent states (S_0, S_2) is stabilized with respect to the (S_1) charge–transfer state (see Scheme 3). This leads to a $S_1 - S_0$ energy gap increase (i.e., absorption blue shift) and a $S_2 - S_1$ decrease. While the S_1/S_0 conical intersection is expected to occur later along S_1 isomerization path, a S_2/S_1 crossing could be generated in this case as found in neutral polyenes [14,55,80,83–91] with a consequent change in the electronic structure of S_1 along the initial part of the path. Thus, while a diradical-type S_1 minimum could exist, an avoided crossing TS could emerge (due to a second S_2/S_1 crossing between the bonding covalent and antibonding ionic surfaces) along the isomerization path (see Scheme 3), which recovers the ionic (charge-transfer) nature of the S_1 state.

CASPT2//CASSCF photoisomerization path computations performed on the ion-pair model systems above,

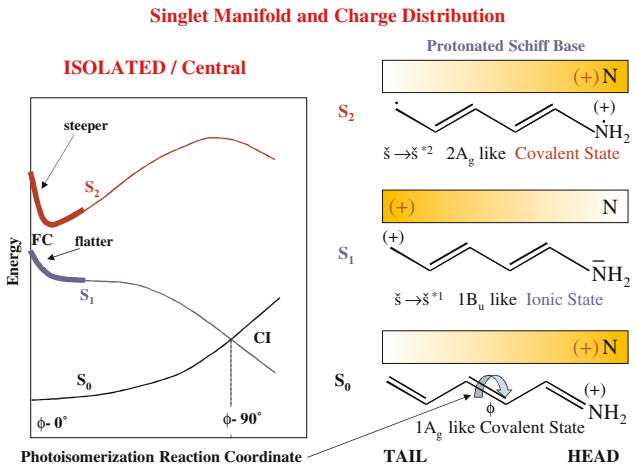

Scheme 1 (From Ref. [79])

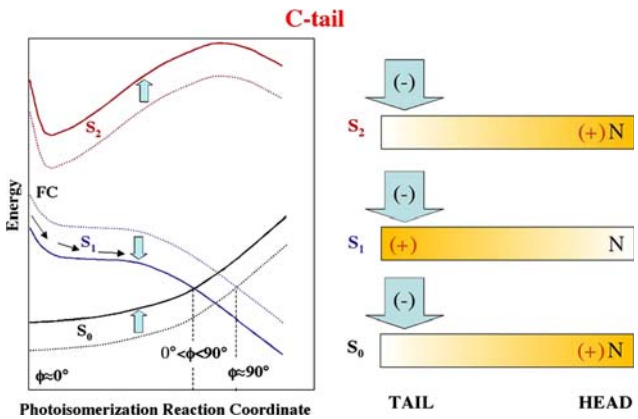

Scheme 2 (From Ref. [79])

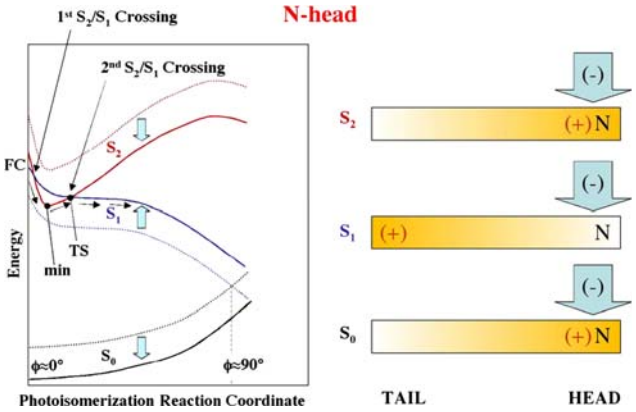

Scheme 3 (From Ref. [79])

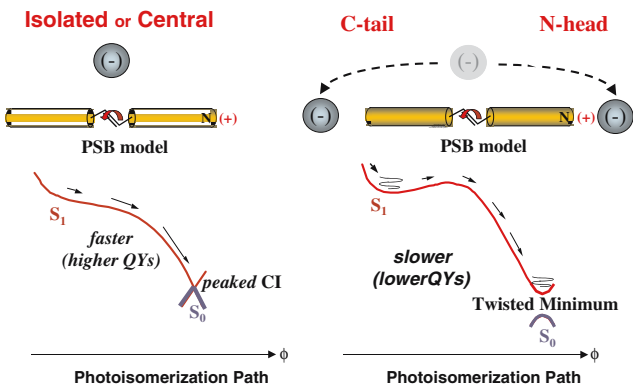

Scheme 4 (From Ref. [79])

demonstrate that such behaviour is indeed found, and the results are consistent with those predicted by the simple electrostatic model above [79].

4.1.3 A unified view for countercharge intermolecular effects

Reaction rate and efficiency control: All the computational results collected for the investigated ion-pairs show that the steepness along the computed photoisomerization MEP and the S_1-S_0 energy gap in the twisted region could be tuned and controlled by the counterion position along the chain. Isolated systems (**1** and **2**) or *Central* models (**1a**, **2a**, and **2b**) display the most favored conditions for ultrafast and efficient central double bond photoisomerizations, namely: (i) steep and/or barrierless isomerization paths, and (ii) TICT conical intersection points of the *peaked* type for internal C–C double-bond flip, funneling an ultrafast and efficient radiationless decay that prompts a high photoisomerization QY. In fact, no thermal equilibration is expected; neither at the initially relaxed planar point on S_1, nor at the degenerate TICT structures. On the other hand, as the countercharge is moved backward to the *C-tail* (**1b**, **2c**) or forward to the *N-head* (**1c**, **2d**) of the system, a slower and less efficient photoisomerization process is expected because: (i) the S_1 PES steepness along the path decreases, (ii) a barrier can possibly emerge, and (iii) *peaked* conical intersections for internal C–C double-bond isomerizations are replaced by twisted minima (with significant energy gap separation between S_1 and S_0) at the bottom of the computed S_1 MEP (see Schemes 1 and 3). Barriers and thermal equilibration at these minima would delay the process, decreasing radiationless decay rate, photoisomerization efficiency and QYs (see Scheme 4).

In conclusion, our results show that the position of the external countercharge can be used as a suitable tool to tune photoisomerization rate and efficiency: only when the countercharge is placed in a *Central* position, or its effects are quenched (i.e., isolated systems), photoisomerization efficiency is magnified and very favored ultrafast (i.e., barrierless) radiationless decay channels are opened. On the other hand, electrostatic interaction with counterions at the *N-head* or the *C-tail* would result (although for different reasons, see discussion above) in slower and less efficient photoisomerizations and radiationless decays.

Photoisomerization stereoselectivity control: Perhaps, one of the most remarkable computational results is that countercharge position does provide a valuable tool to select the double bond likely involved in the photoisomerization process. Moving the counterion above the molecular plane of the chromophore does effect competitive isomerizations for internal C–C double bonds (as seen in models **2a** and **2b**), opening or locking specific isomerization paths: a barrierless (i.e., efficient) photoisomerization leading to a TICT CI point (i.e., an ultrafast radiationless decay funnel) occurs only for the double-bond being closer to the anion (i.e., the double bond right below it), while the other competitive path gets locked, or at least becomes much less favored (i.e., a barrier emerges along the path, and/or the *peaked* CI point disappears being replaced by a twisted minimum, which leads to thermal equilibrations), see Scheme 5.

An even more general result is that the *peaked* CI found in the twisted region *follow* the counterion along the chain of the chromophore, i.e., it involves the rotation of the double bond closer to the anion. This means that highly efficient radiationless decay channels should only exist for photoisomerizations occurring in the vicinity of the countercharge. Anyway, only for the *Central* positions (**1a**, **2a**, and **2b**) the barrierless paths exist (or at least the energy barrier gets negligible), therefore

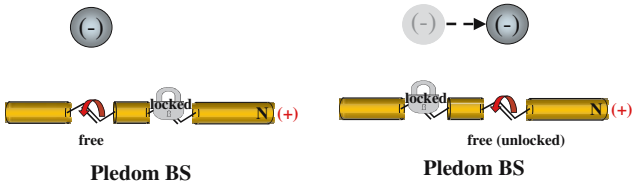

Scheme 5 (From Ref. [79])

opening channels for highly efficient and ultrafast photoisomerizations.

4.1.4 Retinal chromophore in solvent: a QM/MM investigation

The computational results for PSB/counter ion pairs have shown that the influence of an external charge can be quite big. Indeed, it is a well-established experimental result that the environment strongly affects these systems. For example, protein-bound and free-solution chromophores of rhodopsin proteins show different photophysical and photochemical properties [79]. More specifically, the environment may modify the chromophore spectroscopic features and, most important, tune the reaction ratio and control its stereochemistry. For instance, the absorption maximum in the protein (498 and 568 nm for Rh [92] and bR [93], respectively) appears to be red-shifted with respect to the one observed in solution (ca. 440 nm) [94,95]. Furthermore, in Rh (bR) the excited state PSB11 (PSBT) lifetime (following a mono-exponential decay) [96] is ca. 150 fs (200 fs) [97] and its photoisomerization takes place in 200 fs (500 fs) [98,99] leading to the unique *all-trans* PSBT (13-*cis* PSB13) photoproduct with an high 67% (65%) QY [100]. This behavior is different from that observed for the same chromophores in solution (methanol or hexane) where, for instance, excited state lifetime follows a bi-exponential decay [96,101] with a dominant (almost 20 fold longer) 3 ps shorter component [102] and there is a lack of stereospecificity and a decrease in the photoisomerization efficiency (to a low 25% QY) [103,104]. Finally, an excited state energy barrier has been observed for PSBT in solution [101]. It is thus apparent that the protein is able to "catalyze" (i.e., speed up and select) the photoisomerization with respect to the solution environment, and that the solution as well may be very much different than the gas-phase.

In this respect, a major step towards the description of the real system has been very recently achieved through the development and the use of our implementation of a hybrid QM/MM CASPT2//CASSCF/AMBER-GAFF force field that allows complex molecular systems (e.g., biological photoreceptors as well as organic chromophores in solvent) to be investigated at an unprecedented level of accuracy. The objective of our QM/MM implementation is to describe the reactive molecule (e.g., the organic chromophore) at a suitable QM level, and the environment (e.g., the solvent and/or the protein cavity) with a MM force field (for general references on QM/MM methods in the treatment of adiabatic reactions see [105–107]). This method has been used here to investigate the optical properties of the PSB11 chromophore in methanol solution and has been validated by comparison with experimental results.

In order to get the initial geometry of the QM/MM system, an NPT ($P = 1$ atm, $T = 300$ K) molecular dynamics simulation of 1 ns was performed, with the chromophore frozen at its optimized CASSCF/6-31G* geometry and using AM1BCC point charges (partial charges derived from the AM1 wave-function) as the initial guess for the chromophore atoms. A chloride counterion was included and a methanol cube box of 25 Å with periodic boundary conditions was used. After equilibration, one configuration was chosen among those with lower total energy and employed as the initial geometry for QM/MM optimizations.

This system was divided in two parts: (1) the PSB11 chromophore, described at the QM (CASPT2//CASSCF/6-31G*) level and (2) the counterion and the methanol box, described with MM using the AMBER force field. In our two layer (QM + MM) approach, a 10 Å shell of solvent surrounding the Schiff base was fully minimized for each QM step: this procedure allows the chromophore to relax in a movable cavity, embedded in an electrostatic field that rearranges during the optimization.

QM/MM results for the vertical excitation energy (445 nm) show a surprisingly good agreement with the reported experimental value (440 nm) [94,95]. This result underscores the role of solvent on the spectral properties of retinal chromophores and its accuracy provides a validation for our recent implementation of the QM/MM method.

QM/MM computations on Rhodopsin are in progress to investigate the effects of protein environment (both the electrostatic field and the steric/geometric constraints) on the photoisomerization catalysis as well as the possible role of higher lying excited states in the spectroscopic properties of the system.

4.2 Green fluorescent protein chromophore: an exemplary case for environment effects

Several molecular biology and biochemical applications take advantage of the highly fluorescent chromophore, generated auto-catalytically in the green fluorescent

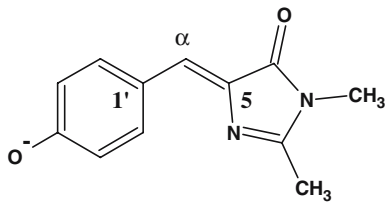

Fig. 5 Structural formula of 4′-hydroxybenzylidene-2,3-dimethyl-imidazolinone, (HBDI) in the anionic state

protein (GFP) from the jellyfish *Aequorea Victorea*. The chromophore, in wild-type GFP, protected from the solvent through the β-can structure formed by the protein [108], exists in two protonation forms, neutral and anionic. The neutral form is responsible for the short-wavelength absorption, at 398 nm, while the anionic form is associated with the long-wavelength peak, at 471 nm [109]. Model chromophores (see Fig. 5) such as 4'-hydroxybenzylidene-2,3-dimethyl-imidazolinone (HBDI) [110] have been employed to compare the vibrational fingerprints of the GFP chromophore in solution and in protein and to investigate the environment effect (protein versus solvent) on the photodynamics of the fluorophore. These studies have shown a dramatic increase in the radiationless decay in solution at room temperature, which results in complete quenching of the fluorescence [111]. In contrast with the excited state dynamics studies, vibrational spectroscopy studies [110,112,113] have shown that the vibrational fingerprints of the chromophore are quite similar in solution and in the protein. Overall, the experimental data show how the molecular properties (spectroscopic features, photoreactivity, etc.) of the GFP chromophore respond in different ways to the environment. A suitable theoretical model must be able to predict with similar quality, environment effects on various molecular properties. In a recent study, we have investigated solvent effects on the spectroscopy and photoreactivity of the anionic form of the GFP chromophore and have shown how structural modifications induced by the solvent affect at the same time vibrational activities and deactivation channels [19].

4.2.1 Vibrational activities

The model chromophore considered, HBDI (see Fig. 5), includes the complete conjugate system of the real GFP chromophore and it is the chromophore investigated in solution in several vibrational studies [110,113,114]. The vibrational spectra were simulated in vacuo and by including the solvent effect (water, since this was used to measure the experimental Raman spectra [110]) through the polarizable continuum model (PCM) [27–29]. Molecular parameters required to model vibronic structures were obtained at HF (for S_0) and CIS (for S_1) levels of theory, a procedure that ensures reliable results as proven by several previous investigations [115,116]. Notice that since RR intensities are directly related to the displacement of the excited state potential energy surface (PES) with respect to the ground state, the comparison between observed and simulated intensities validates at the same time the quality of the predicted relaxed structures in S_0 and S_1.

The RR spectra, in vacuo and by inclusion of solvent effects, simulated according to the models described in Ref. [117–119], show a trend similar to the off-resonance Raman spectra [19]. The RR spectrum predicted in vacuo for the anionic form (see Fig. 6 for a comparison between computed and experimental spectra [113]) is similar to the predicted off resonance Raman spectrum [19] but it disagrees remarkably with the observed spectrum. Inclusion of solvent effects improves significantly the agreement with experiment. Notice that this improvement implies that the solvent and in vacuo predicted S_0–S_1 geometry changes must be rather different for the anionic chromophore. Indeed, similar

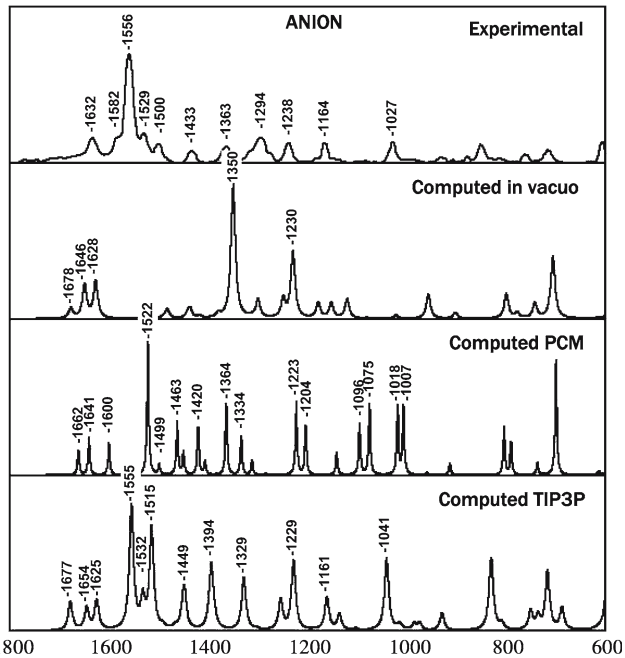

Fig. 6 Resonance Raman spectra (from HF and CIS calculations) of the HBDI chromophore, simulated in vacuo and in water with implicit solvent (PCM approach) and with explicit solvent molecules (QM/MM approach) and comparison with the correspondingly observed experimental spectrum from Ref. [113]. From *top to bottom*: experimental, computed in vacuo (6-31+G* basis set), with implicit water included (6-31+G* basis set), with explicit water included (6-31G* basis set). Frequencies were uniformly scaled by 0.9

to the ground state, the excited state geometry also is affected by solvent effects, and dominant changes occur in the exocyclic CC bonds. More important, the solvent modifies (with respect to gas phase) the ground state and excited state exocyclic bonds in an *opposite way*. Indeed, in solvated S_1 the CαC5 bond (double bond in the ground state) is elongated with respect to gas phase S_1, while the C1'Cα bond (single bond in the ground state) is shortened in the solvent with respect to the gas phase. Bond lengths changes upon solvation, go in the opposite direction in the ground state. As a result, inclusion of solvent effects induces an $S_1 - S_0$ geometry change, in which the two exocyclic CC bond lengths are modified in opposite ways: the CC single bond shortens upon excitation, while the CC double bond lengthens upon excitation.

The exocyclic bond length changes upon excitation predicted in solvent (*out of phase* geometry change) and in vacuo (*in phase* geometry change), imply remarkably different RR intensities in the two situations, since among the Raman active modes, intensity will be enhanced for those modes that mimic the $S_1 - S_0$ geometry change. This effect is exemplified in Fig. 7. Specifically, the 1,522 cm^{-1} frequency normal mode, which shows the largest RR intensity in the simulations with solvent (see Fig. 6), is indeed characterized by an *out of phase* motion of the two exocyclic CC bonds. The same vibrational mode cannot be active in vacuo where activity is enhanced, on the contrary, for the mode with frequency 1,350 cm^{-1}, characterized by an *in phase* motion of the two exocyclic CC bonds. The effects discussed above are confirmed also at CASSCF(12,11)/6-31G* level of theory used for subsequent PES (MEPs) calculations.

QM/MM explicit solvent calculations: The initial configuration for the QM/MM system, formed by the HBDI anionic chromophore with a sodium counterion, in a TIP3P water box of 16 Å, was obtained from an NPT molecular dynamics simulations of 1 ns ($P = 1$ atm, $T = 300$ K), with the chromophore frozen at its optimized CASSCF/6-31G* geometry. During the MD equilibration, the positive counterion diffused into the solvent. In the following QM/MM calculations, the HBDI chromophore was described at the QM level, and the water box was described with MM (TIP3P rigid model). A three layer approach was adopted ($QM + MM_1 + MM_2$), with the first 3 Å shell of water molecules surrounding the chromophore (MM_1) optimized together with the QM chromophore, and a further 7 Å shell of solvent molecules (MM_2) surrounding the first shell, fully minimized for each $QM + MM_1$ step.

The resulting ground state structure of the chromophore was obtained either at CASSCF(12,11)/6-31G* or

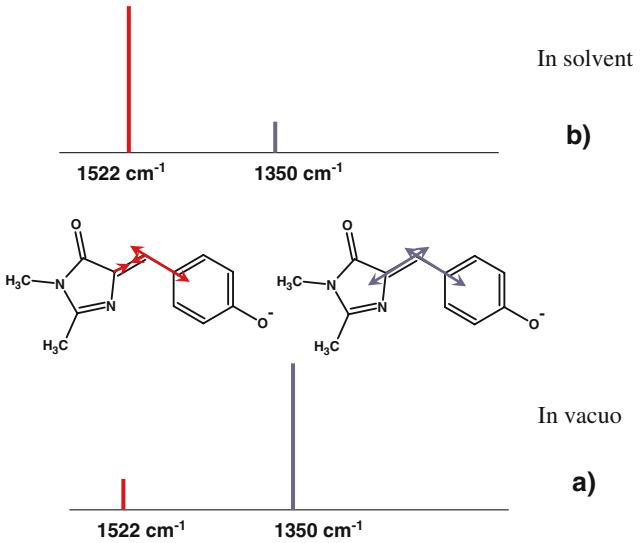

Fig. 7 Schematic representation of the selective enhancement of active modes for the anionic form of HBDI through the RR mechanism: **a** in vacuo: the $S_1 - S_0$ geometry change is dominated by the in phase variation of the exocyclic CC bonds, and the band at 1,350 cm^{-1} is selectively enhanced in the RR spectrum schematically shown at the bottom; **b** in solvent: the $S_1 - S_0$ geometry change is dominated by the out of phase variation of the exocyclic CC bonds, and the band at 1,522 cm^{-1} is selectively enhanced in the RR spectrum schematically shown at the top (adapted from Ref. [19])

HF/6-31G* levels of theory. The geometry change, with respect to vacuo is similar to that computed at PCM level [19], and to that documented in a recent study also based on a QM/MM scheme [120]. The RR spectrum simulated using HF (for S_0) and CIS(for S_1) molecular parameters, reported at the bottom of Fig. 6, is in remarkable agreement with the experimental data. These results provide an additional validation for our QM/MM implementation and show that very satisfactory RR intensity predictions can be obtained at relatively inexpensive levels of theory.

4.2.2 Optical spectra

As discussed in the previous section, the PCM correction modifies the FC (i.e., ground state) structure with respect to gas phase calculations. In this regard, it is interesting to compare the CASPT2 computed vertical excitation at this FC structure, with the experimental data. Calculations predict a vertical excitation of 461 nm, as compared with the 425–432 nm [110,113] observed in water. Notice that the CASPT2 calculations include the solvent effects only on the CASSCF part, and their contribution is to increase the vertical excitation energy from 493 nm (in vacuo) to 461 nm. It can be expected that also the PT2 contribution goes in the same direction,

and this would lead to an even better agreement with the experimental data. Furthermore, the change in dipole moment upon excitation, computed with the PCM corrected wave functions is 8.6 D, in close agreement with the value and the direction of the observed change of 6.8 D [121].

We have also estimated vertical excitation energies with the QM/MM scheme. The result (441 nm) is in good agreement with the reported experimental values (425–432 nm) [110,113], featuring an error of ca. 2 kcal/mol. The vertical excitation computed at the same structure but in vacuo is 539 nm, showing that the electrostatic contribution from the solvent is ca. 12 kcal/mol. Notice that such contribution is strongly dependent on the ground state structure, and it decreases to less than 2 kcal/mol for a structure close to that optimized in vacuo. The computed vertical excitation energies are obtained from single state, rather than state-average CASSCF calculations. This explains the slightly lower value of the absorption maximum computed here compared with that reported in ref. [120].

To further validate our QM/MM model, we have also evaluated the 0–0 excitation energy in protein corresponding to the I state of wt-GFP, in the three state model [122]. The initial structure of the system was obtained from the X-ray structure 1GFL from the PDB archive. Monomer A was chosen and the chromophore structure (QM part, same structure of the HBDI chromophore) and three water molecules (MM part treated at TIP3P level) were optimized, whilst the remaining of the protein was kept frozen at the geometry of the crystal structure. Despite the simplified scheme adopted here, in comparison to ref. [120], the computed 0–0 energy (533 nm) is in good agreement with the experimental value (495 nm [122]).

4.2.3 Photoreactivity

The remarkable solvent effect on both S_0 and S_1 relaxed structures, responsible for the dramatic difference between Raman intensities in vacuo and in solvent, has also implications on the photodynamics of the anionic HBDI chromophore, since the relaxation of the S_1 state from the vertical FC structure (ground state equilibrium geometry) to the optimized or fluorescent state (FS) structure, represents the first step of the two-state/two mode deactivation path of the excited chromophore. Furthermore, the different FS structure in solvent, as compared with the gas phase influences the preferential channel of ultrafast radiationless deactivation, characterizing the second step of the photoreaction. As a result, it can be stated that the discrepancy between in vacuo simulated and experimental Raman spectra of anionic HBDI in solution [110,113], implies also that the deactivation path predicted in vacuo [123] does not represent the preferential deactivation channel in solution.

Owing to the markedly delocalized exocyclic chromophore structure in the excited state, the PCM corrected PES (see Fig. 8), in the FS region, is remarkably flat. From the FS region, the system can evolve in several different ways: (1) it can deactivate radiatively or it can rotate around the two exocyclic CC bonds to produce (2) a twisted intermediate TW2 if rotation occurs around the CC bond which is markedly double in the ground state, leading to the double bond flip mechanism, (3) a twisted intermediate TW1 for rotation around the other CC bond, mainly single in the ground state, leading to a single bond flip mechanism and (4) a hula-twist intermediate HT if simultaneous rotation around both exocyclic bonds occurs.

Owing to the high energy of the HT structure (11 kcal/mol above the FS structure), it is highly unlikely that the HT plays a role in the deactivation of the excited state in solution. Conversely, the rotation around either one of the exocyclic CC bonds leads to the intermediates TW1 and TW2, both characterized by an energy lower than the FS structure (see Fig. 8). The calculations of the photoreaction path do not indicate a preferential initial channel of deactivation, in contrast with gas phase calculations [123] since rotation around the two CC exocyclic bonds is almost barrierless for both channels.

However, after this region, the energy starts lowering significantly. The TW1 intermediate is computed to be about 5 kcal/mol lower in energy than the FS structure at CASPT2 level, while the TW2 intermediate is even more stable: 13 kcal/mol. More important, the energy gap between S_0 and S_1 is significant for the TW1 structure: 32 kcal/mol at CASPT2 level, as a result of the moderate energy increase of the ground state when the CC single bond is twisted. The large gap suggests that the TW1 channel, in solution, is unlikely to be responsible for the fast IC experimentally documented. Conversely, the $S_0 - S_1$ gap is remarkably reduced at the TW2 structure: 6 kcal/mol at CASPT2 level, owing to the considerable energy increase of the ground state when rotating around the exocyclic CC double bond. Such a small energy gap is compatible with a real crossing in the surrounding region and, consequently, with an efficient radiationless decay. For this reason, the TW2 channel is identified as the dominant radiationless deacay route of the photoexcited anionic chromophore in solution. Notice that the negative charge in the excited state is almost completely localized on the imidazolinone ring, for the TW1 structure, and on the phenolic ring for the

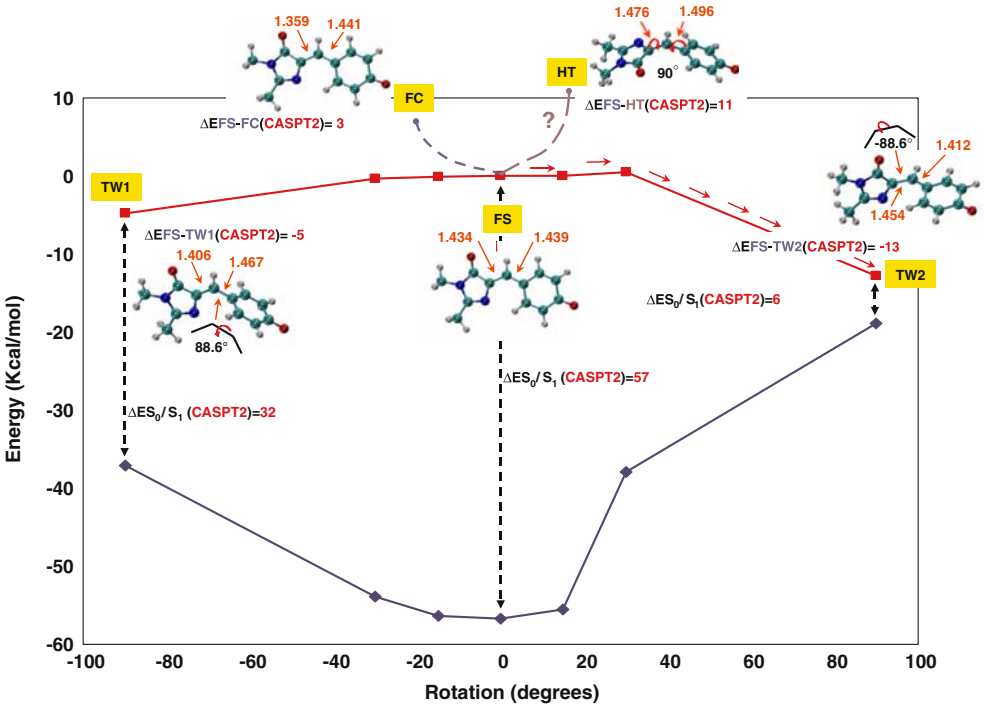

Fig. 8 CASPT2 energy profiles for the electronic S_1 and S_0 states of the anionic form of HBDI in solvent, along the computed FS → TW1 and FS → TW2 relaxation coordinates. CASPT2 and CASSCF relative energies are in kcal/mol. The stream of arrows indicates the reaction path responsible for ultrafast radiationless decay (adapted from ref. [19])

TW2 structure. The charge localization is completely reversed in the ground state.

Rotation around the exocyclic double bond leads to *cis–trans* photoisomerization (with a consequent variation of the ground state *cis* and *trans* populations), an observation that has been experimentally documented [124].

Protein effect: In contrast with the synthetic model chromophores in solution, the protein environment suppresses dramatically the radiationless decay. Based on the results of the solution study we may suggest one plausible reason for the suppression of fluorescence in protein, namely the reduced efficiency of the TW2 radiationless decay channel which is strongly favored in solution and would be strongly hampered in the protein. The exocyclic chromophore structure in S_0 and S_1, determined in a recent QM/MM study of the chromopore in protein [120], with the protein structure in the B state [122] is quite similar to that of the solvated chromophore obtained with PCM corrected calculations [19]. Thus, it can be assumed that the photoreaction path computed, including solvent effects is a reasonable starting point to discuss the photoreactivity in protein. In the light of the predominant decay mechanism established in solution, we can speculate on what can be the effect of protein on it. We can envisage at least three reasons for suppression of this decay cannel. First, the exocyclic CC double bond torsion will be strongly hindered for steric reasons. Second, the breaking of the hydrogen bond between water W22 and the phenolic oxygen of the chromophore will also contribute to suppress this channel. Both these factors would induce a relevant barrier along the torsional reaction coordinate. A third factor is attributed to electrostatic interactions. Indeed, the negative charge is localized, for the TW2 intermediate, on the phenolic ring. In contrast, a positive charge (ARG96) is located, in the protein, close to the ammidic oxygen of the chromophore. Thus, it may be expected that the reaction path involving translocation of the negative charge from the imidazolinone to the phenolic ring (namely the TW2 reaction path) will be strongly disfavored in protein.

5 Concluding remarks

We have discussed the photophysical and photochemical behavior of three widely-studied chromophores, namely azobenzene, retinal protonated Schiff base and GFP chromophore, stressing in particular the effect of structural modifications and environment perturbations on their properties.

For Ab, we have analyzed the mechanism by which S_1 and S_2 decay to the ground state bringing about *cis–trans* isomerization. We have shown, by means of MEPs

calculations, that the two states decay following different routes and give different photoisomerization quantum yields, violating the Kasha's rule. We have considered the effects of the reduction of the π system size of Ab by studying CPD. Quite surprisingly, this modified molecule shows only minor changes in the mechanisms and quantum yields of the S_1 and S_2 decay.

We have found that the presence of an anion in the proximity of the retinal chromophore strongly modifies its photohysical and photochemical behavior. The type of changes depends sharply on the specific location of the countercharge. Based on these results and on the simple electrostatic model shown, we have provided a simple rationale for the high rate and photoisomerization efficiency seen in rhodopsin proteins with respect to retinal, and for the control of their stereochemistry.

Similarly, GFP is found to lock photoisomerization channels and to lead to much longer living excited states, which do fluoresce, than the free-solution GFP chromophore. These observations have been rationalized here in terms of MEPs calculations and of their modifications in the presence of the environment. Furthermore, the simultaneous rationalization of its RR activity and photoreactivity in solution, accounted for only after the inclusion of solvent effects, represents an exemplary case of severe interplay between photophysical and photochemical behavior. Indeed it has been shown that the structural modifications induced by the solvent on both ground and excited states of the anionic GFP chromophore affect, on one side the vibrational structure and, on the other side, the deactivation channels of the photoexcited state.

Although we are still at the beginning in the rationalization of environment effects, the examples discussed in this work indicate that stronger effects can be expected preferentially from polar (or locally charged) environments. On the other hand, to increase the response of the chromophore to the environment, changes in the electron distributions, such as those induced by the introduction of electron–donor or -acceptor groups, are in order. The results on azobenzene underscore this latter point, since stronger polar perturbations than those discussed here would be required to modify significantly its photochemistry. In contrast, the retinal and GFP chromophores, fulfill the basic requirement of an asymmetric electron distribution and the results discussed here demonstrate how a finer tuning of their photophysical–photochemical properties might be obtained by more subtle structural changes.

Acknowledgements This work was supported by funds from MURST PRIN 2004 (project: "Spettroscopia rotazionale in assorbimento e a trasformate di Fourier: Produzione e studio di nuovi cluster e specie molecolari in espansioni supersoniche"), MURST PRIN 2005 (project: "Trasferimenti di energia e di carica a livello molecolare"), MURST ex 60% (Project: "Modelli per lo studio delle proprietà di sistemi molecolari complessi") FIRB 2001 (projects n. RBNE019NKS and RBAU01L2HT) and the University of Bologna (Funds for Selected Research Topics).

References

1. Drexler KE (1986) Engines of creation: the coming era of nanotechnology. Anchor Books Editions, USA
2. Dugave C, Demange L (2003) Chem Rev 103:2475
3. Tamai N, Miyasaka H (2000) Chem Rev 100:1875–1890
4. Yokoyama Y (2000) Chem Rev 1000:1717–1739
5. Irie M (2000) Chem Rev 100:1685–1716
6. Fuss W, Lochbrunner S, Muller AM, Schikarski T, Schmid WE, Trushin SA (1998) Chem Phys 232:161–174
7. Gonzalez-Luque R, Garavelli M, Bernardi F, Merchan M, Robb MA, Olivucci M (2000) Proce Nat Acad Sci USA 97:9379–9384
8. Truhlar DG, Gordon MS (1990) Science 249:491
9. Ciminelli C, Granucci G, Persico M (2004) Chem Eur J 10:2327–2341
10. Toniolo A, Ciminelli C, Persico M, Martinez TJ (2005) J Chem Phys 123:234308
11. Fuss W, Kompa KL, Lochbrunner S, Muller AM (1997) Chem Phys Physi Chem 101:500–509
12. Natansohn A, Rochon P (2002) Chem Rev 102:4139
13. Hampp N (2000) Chem Rev 100:1755
14. Garavelli M, Celani P, Fato M, Bearpark MJ, Smith BR, Olivucci M, Robb MA (1997) J Phys Chem A 101:2023–2032
15. Celani P, Robb MA, Garavelli M, Bernardi F, Olivucci M (1995) Chem Phys Lett 243:1–8
16. Bearpark MJ, Robb MA, Schlegel HB (1994) Chem Phys Lett 223:269–274
17. Gonzalez C, Schlegel HB (1990) J Phys Chem 94:5523
18. Cembran A, Bernardi F, Garavelli M, Gagliardi L, Orlandi G (2004) J Am Chem Soc 126:3234–3243
19. Altoe P, Bernardi F, Garavelli M, Orlandi G, Negri F (2005) J Am Chem Soc 127:3952–3963
20. Andersson K, Malmqvist P-Å, Roos BO (1992) J Chem Phys 96:1218
21. McDouall JJW, Peasley K, Robb MA (1988) Chem Phys Lett 148:183–189
22. Roos BO (1980) Int J Quant Chem 14:175
23. Roos BO, Taylor PR, Siegbahn PEM (1980) Chem Phys 48:157
24. Roos BO (1987) In: Lawley KP (ed) Ab initio methods in quantum chemistry - II Wiley, New York, p. 399–446
25. Siegbahn PEM, Almlof J, Heiberg A, Roos BO (1981) J Chem Phys 74:2384
26. Bernardi F, Olivucci M, Robb MA (1996) Chem Soc Rev 25:321
27. Cossi M, Barone V, Cammi R, Tomasi J (1996) Chem Phys Lett 255:327–335
28. Mennucci B, Tomasi J (1997) J Chem Phys 106:5151–5158
29. Tomasi J, Cammi R, Mennucci B, Cappelli C, Corni S (2002) Phys Chem Chem Phys 4:5697–5712
30. Vreven T, Byun KS, Komaromi I, Dapprich S, Montgomery JA, Morokuma K, Frisch MJ (2006) J Chem Theory Comput 2:815–826
31. Cornell WD, Cieplak P, Bayly CI, Gould IR, Merz KM, Ferguson DM, Spellmeyer DC, Fox T, Caldwell JW, Kollman PA (1995) J Am Chem Soc 117:5179–5197

32. Wang JM, Wolf RM, Caldwell JW, Kollman PA, Case DA (2004) J Comput Chem 25:1157–1174
33. Fischer E, Malkin S (1962) J Phys Chem 66:2482
34. Rau H, Luddeke E (1982) J Am Chem Soc 104:1616
35. Rau H, (1990) In: Dürr H, Bounas-Laurent H (eds) Photocromism, molecules and systems. Elsevier, Amsterdam, p. 165–192
36. Fujino T, Arzhantsev SY, Tahara T (2001) J Phys Chem A 105:8123–8129
37. Bortolus P, Monti S (1979) J Phys Chem 83:648
38. Siampiringue N, Guyot G, Bortolus P, Monti S (1987) 37:185
39. Cattaneo P, Persico M (1999) Phys Chem Chem Phys 1:4739
40. Ishikawa T, Noro T, Shoda T (2001) J Chem Phys 115:7503
41. Gagliardi L, Orlandi G, Bernardi F, Cembran A, Garavelli M (2004) Theor Chem Acc 111:363–372
42. Diau EWG (2004) J Phys Chem A 108:950–956
43. Birks JB (1970) Photophysics of aromatic molecules, Wiley, London
44. Kubo R, Toyozawa Y (1955) Prog Theor Phys 13:160–182
45. Brown EV, Grunneman GR (1975) J Am Chem Soc 97:621
46. Lednev I, Ye TQ, Matousek P, Townie M, Foggi P, Neuwahl F, Umapathy S, Moore J (1998) Chem Phys Lett 290:68
47. Pierloot K, Dumez B, Widmark P-O, Roos BO (1995) Theor Chim Acta 90:87
48. Kandori H, Shichida Y, Yoshizawa T (2001) Biochem Mosc 66:1197–1209
49. Needleman R (1995) In: Horspool WM, Song P-S (eds) CRC handbook of organic photochemistry and photobiology. CRC Press, Boca Raton, p. 1508–1515
50. Ottolenghi M, Sheves M (1995) Isr J Chem 35:U3–U3
51. Wald G, (1968) Science 162:230–239
52. Mathies R, Lugtenburg J (2000) In: Stavenga DG, DeGrip WJ, Pugh ENJ (eds) Molecular mechanism of vision. Elsevier, New York p. 55–90
53. Yoshizawa T, Kuwata O (1995) In: Horspool WM, Song P-S (eds) CRC handbook of organic photochemistry and photobiology. CRC Press, Boca Raton, p. 1493–1499
54. Garavelli M, Celani P, Bernardi F, Robb MA, Olivucci M (1997) J Am Chem Soc 119:6891–6901
55. Garavelli M, Bernardi F, Olivucci M, Vreven T, Klein S, Celani P, Robb MA (1998) Faraday Discuss 110:51–70
56. Garavelli M, Vreven T, Celani P, Bernardi F, Robb MA, Olivucci M (1998) J Am Chem Soc 120:1285–1288
57. De Vico L, Page CS, Garavelli M, Bernardi F, Basosi R, Olivucci M (2002) J Am Chem Soc 124:4124–4134
58. Ruhman S, Hou BX, Friedman N, Ottolenghi M, Sheves M (2002) J Am Chem Soc 124:8854–8858
59. Garavelli M, Bernardi F, Celani P, Robb MA, Olivucci M (1998) J Photochem Photobiolo Chem 114:109–116
60. Garavelli M, Negri F, Olivucci M (1999) J Am Chem Soc 121:1023–1029
61. Cembran A, Bernardi F, Olivucci M, Garavelli M (2003) J Am Chem Soc 125:12509–12519
62. Albeck A, Livnah N, Gottlieb H, Sheves M (1992) J Am Chem Soc 114:2400
63. Teller DC, Okada T, Behnke CA, Palczewski K, Stenkamp RE (2001) Biochem 40:7761–7772
64. Kobayashi T, Saito T, Ohtani H (2001) Nature 414:531–534
65. Hou B, Friedman N, Ruhman S, Sheves M, Ottolenghi M (2001) J Phys Chem B 105:7042–7048
66. Haran G, Morlino EA, Matthes J, Callender RH, Hochstrasser RM (1999) J Phys Chem A 103:2202–2207
67. Logunov SL, Volkov VV, Braun M, El-Sayed MA (2001) Proce Nat Acad Sci USA 98:8475–8479
68. Kandori H, Furutani Y, Nishimura S, Shichida Y, Chosrowjan H, Shibata Y, Mataga N (2001) Chem Phys Lett 334:271–276
69. Weiss RM, Warshel A (1979) J Am Chem Soc 101:6131–6133
70. Sheves M, Kohne B, Mazur J (1983) J Chem Soc Chem Commun 1232–1234
71. Sheves M, Nakanishi K, Honig B (1979) J Am Chem Soc 101:7086–7088
72. Nakanishi K, Balogh-Nair V, Arnaboldi M, Tsujimoto K, Honig B (1980) J Am Chem Soc 102:7945–7947
73. Motto MG, Sheves M, Tsujimoto K, Balogh-Nair V, Nakanishi K (1980) J Am Chem Soc 102:7947–7949
74. Honig B, Dinur U, Nakanishi K, Balogh-Nair V, Gawinowicz MA, Arnaboldi M, Motto MG (1979) J Am Chem Soc 101:7084–7086
75. Honig B, Greenberg AD, Dinur U, Ebrey TG (1976) Biochem 4593
76. Birge RR, Hubbard LM (1980) J Am Chem Soc 102:2195–2205
77. Michl J, Bonacic-Koutecky V (1990) Electronic aspects of organic photochemistry. J Wiley, New York
78. Bonacic-Koutecky V, Koutecky J, Michl J (1987) Angew Chem Inte Edi 26:170–189
79. Cembran A, Bernardi F, Olivucci M, Garavelli M (2004) J Am Chem Soc 126:16018–16037
80. Fuss W, Haas Y, Zilberg S (2000) Chem Phys 259:273–295
81. Strodel P, Tavan PJ (2002) Chem Phys 117:4677
82. Nakayama K, Nakano H, Hirao K (1998) Int J Quant Chem 66:157
83. Hudson BS, Kohler BE, Schulten K (1982) Excited states. Academic Press, New York, p. 1–99
84. Klessinger M, Michl J (1994) Excited states and photochemistry of organic molecules, VCH, New York
85. Celani P, Garavelli M, Ottani S, Bernardi F, Robb MA, Olivucci M (1995) J Am Chem Soc 117:11584–11585
86. Robb MA, Garavelli M, Olivucci M, Bernardi F (2000) Rev Comput Chem 15:87–146
87. Garavelli M, Smith BR, Bearpark MJ, Bernardi F, Olivucci M, Robb MA (2000) J Am Chem Soc 122:5568–5581
88. Garavelli M, Celani P, Bernardi F, Robb MA, Olivucci M (1997) J Am Chem Soc 119:11487–11494
89. Garavelli M, Frabboni B, Fato M, Celani P, Bernardi F, Robb MA, Olivucci M (1999) J Am Chem Soc 121:1537–1545
90. Garavelli M, Page CS, Celani P, Olivucci M, Schmid WE, Trushin SA, Fuss W (2001) J Phys Chem A 105:4458–4469
91. Garavelli M, Bernardi F, Olivucci M, Bearpark MJ, Klein S, Robb MA (2001) J Phys Chem A 105:11496–11504
92. Wald G, Brown PK (1958) Science 127:222
93. Rehorek M, Heyn MP (1979) Biochemistry 18:4977
94. Freedman KA, Becker RS (1986) J Am Chem Soc 108:1245–1251
95. Bachilo SM, Bondarev SL, Gillbro T (1996) J Photochem Photobiolo B Biology 34:39–46
96. Hamm P, Zurek M, Roschinger T, Patzelt H, Oesterhelt D, Zinth W (1996) Chem Phys Lett 263:613–621
97. Kandori H, Sasabe H, Nakanishi K, Yoshizawa T, Mizukami T, Shichida Y (1996) J Am Chem Soc 118:1002–1005
98. Schoenlein RW, Peteanu LA, Mathies RA, Shank CV (1991) Science 254:412–415
99. Mathies RA, Cruz CHB, Pollard WT, Shank CV (1988) Science 240:777–779
100. Dartnall HJA (1967) Vis Res 8:339–358
101. Logunov SL, Song L, ElSayed MA (1996) J Phys Chem 100:18586–18591
102. Kandori H, Katsuta Y, Ito M, Sasabe H (1995) J Am Chem Soc 117:2669–2670
103. Becker RS, Freedman KA (1985) J Am Chem Soc 107:1477–1485

104. Koyama Y, Kubo K, Komori M, Yasuda H, Mukai Y (1991) Photochem Photobiolo 54:433–443
105. Pu JZ, Gao JL, Truhlar DG (2004) J Phys Chem A 108:632–650
106. Gao JL, Truhlar DG (2002) Ann Rev Phys Chem 53:467–505
107. Mo YR, Alhambra G, Gao JL (2000) Acta Chimi Sin 58:1504–1510
108. Ormo M, Cubitt AB, Kallio K, Gross LA, Tsien RY, Remington SJ (1996) Science 273:1392–1395
109. Chattoraj M, King BA, Bublitz GU, Boxer SG (1996) Proc Natl Acad Sci USA 93:8362–8367
110. He XA, Bell AF, Tonge PJ (2002) J Phys Chem B 106:6056–6066
111. Niwa H, Inouye S, Hirano T, Matsuno T, Kojima S, Kubota M, Ohashi M, Tsuji FI (1996) Proc Natl Acad Sci USA 93:13617–13622
112. Bell AF, He X, Wachter RM, Tonge PJ (2000) Biochemistry 39:4423–4431
113. Schellenberg P, Johnson E, Esposito AP, Reid PJ, Parson WW (2001) J Phys Chem B 105:5316–5322
114. Esposito AP, Schellenberg P, Parson WW, Reid PJ (2001) J Mol Struct 569:25–41
115. Negri F, Zgierski MZ (1992) J Chem Phys 97:7124–7136
116. Negri F, Zgierski MZ (1993) J Chem Phys 99:4318–4326
117. Negri F, Orlandi G (1997) J Photoch Photobio A 105:209–216
118. Negri F, Orlandi G (1995) J Chem Phys 103:2412–2419
119. Negri F, Orlandi G (2005) In: Olivucci M (ed) Computational photochemistry. Elsevier, Amsterdam, p. 129–169
120. Sinicropi A, Andruniow T, Ferre N, Basosi R, Olivucci M (2005) J Am Chem Soc 127:11534–11535
121. Bublitz G, King BA, Boxer SG (1998) J Am Chem Soc 120:9370–9371
122. Creemers TMH, Lock AJ, Subramaniam V, Jovin TM, Volker S (1999) Nature Struct Biol 6:557–560
123. Martin ME, Negri F, Olivucci M (2004) J Am Chem Soc 126:5452–5464
124. He X, Bell AF, Tonge PJ (2003) FEBS Lett 549:35–38
125. Garavelli M, Bernardi F, Robb MA, Olivucci M (2002) Int J Photoenergy 4:57–68